Volume 12 | Number 11 | 7 June 2025

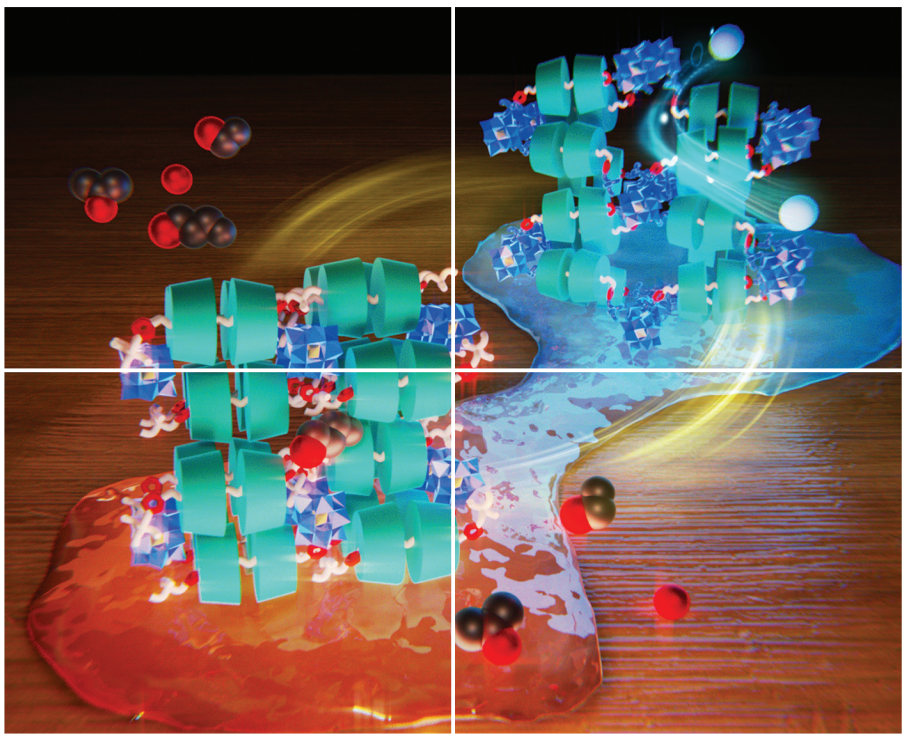

INORGANIC CHEMISTRY

FRONTIERS

CCS 中国化学会 CHINESE CHEMICAL SOCIETY

PEKING UNIVERSITY 1898

ROYAL SOCIETY OF CHEMISTRY

rsc.li/frontiers-inorganic

INORGANIC CHEMISTRY FRONTIERS

RESEARCH ARTICLE

View Article Online
View Journal | View Issue

Cite this: *Inorg. Chem. Front.*, 2025, **12**, 3800

Nanocluster-regulated porous ionic rotaxane assemblies with solvent-adaptability for selective adsorption and conductivity†

Jiaxu Wang, Mingfeng Wei, Zexi Zhu, Bao Li * and Lixin Wu *

Received 22nd February 2025,
Accepted 9th April 2025

DOI: 10.1039/d5qi00535c

rsc.li/frontiers-inorganic

Porous supramolecular assemblies are increasingly recognized for their capabilities in mass transfer and selective loading and release. In this study, a dicationic cyclodextrin[3]rotaxane was synthesized to exhibit adaptivity in the flexible motion between the macrocycle and axle, allowing dynamic structural adjustment during their co-assembly with polyanionic nanoclusters. Meanwhile, the anions regulate the assembly to form layered, fibrous, and porous structures. By simply mixing the charged components in solution, porous ionic rotaxane-cluster assemblies have been prepared, showing selective adsorption and adaptive structural transformations. These assemblies exhibit a "breathing" effect in response to solvent adsorption/desorption, thereby enabling ABE mixture separation. DMSO disrupts hydrogen bonds and ionic interactions, allowing recrystallization to form a porous structure with larger pores. This transition is reversible by returning to the original structure in aqueous solution. The reorganization can change proton conductivity by about three orders between the two structures.

1. Introduction

Porous supramolecular assemblies exhibit a large specific surface area for mass transportation and selective loading, making them promising for wide applications in chemistry, materials science, and medicine.[1–3] By ingenious design of building blocks and controlling of interactions, it is possible to modify the pore structure and achieve various surface properties and additional material characteristics. Coordination bonds,[4] dynamic covalent bonds,[5] hydrogen bonds,[6] and other directional intermolecular interactions,[7–10] have been extensively used to construct porous supramolecular assemblies. However, despite the unique properties of ionic interactions, the research on porous structures dominated by ionic bonds still lags far behind the achievements of other porous supramolecular assemblies.

Porous ionic assemblies are simpler to prepare and more renewable compared to coordination/covalent porous assemblies.[11,12] The high-density permanent charges in the pores confer unique physicochemical properties.[13] Due to long-range coulombic interactions, these ionic assemblies can demonstrate a certain degree of structural flexibility.[14] However, the lack of directionality in coulombic interactions between ions makes the rational design of building blocks particularly challenging for controlling orientation and inducing synergistic effects.[15] Polyoxometalates (POMs) are a class of large anionic nanoclusters of uniform size with a variety of properties.[16–18] Incorporating POMs into porous ionic assemblies not only serves as a key node to support the pore structure but also enriches the material's functionality, expanding potential applications of these nanoclusters.[19] Currently, porous ionic assemblies are mainly constructed through the following approaches: (i) organic bases and acids (commonly referred to as crystalline porous organic salts, or CPOSs) are used to construct the framework structure through directional ionic bonds, following the principles of reticular chemistry;[20–22] (ii) POMs and metal coordination cations (commonly referred to as porous ionic crystals, or PICs) form porous structures composed of 0D spherical particles;[23,24] (iii) POMs and organic bridge-linked cations (commonly referred to as supramolecular ionic frameworks or SIFs) also follow the principles of reticular chemistry.[25–31]

In the construction of SIFs, it is known that the framework formation relies on the support of hydrogen bonds and spatial suitability with the corresponding cations, thereby addressing the inherent directional control in ionic interactions. However, the design of large cationic building blocks that match the POMs and the precise structural characterization of the resulting porous structures pose key challenges in supporting this

State Key Laboratory of Supramolecular Structure and Materials, College of Chemistry, Jilin University, Changchun 130012, China. E-mail: wulx@jlu.edu.cn, libao@jlu.edu.cn

† Electronic supplementary information (ESI) available. CCDC 2320351–2320357, 2421014 and 2421017–2421019. For ESI and crystallographic data in CIF or other electronic format see DOI: https://doi.org/10.1039/d5qi00535c

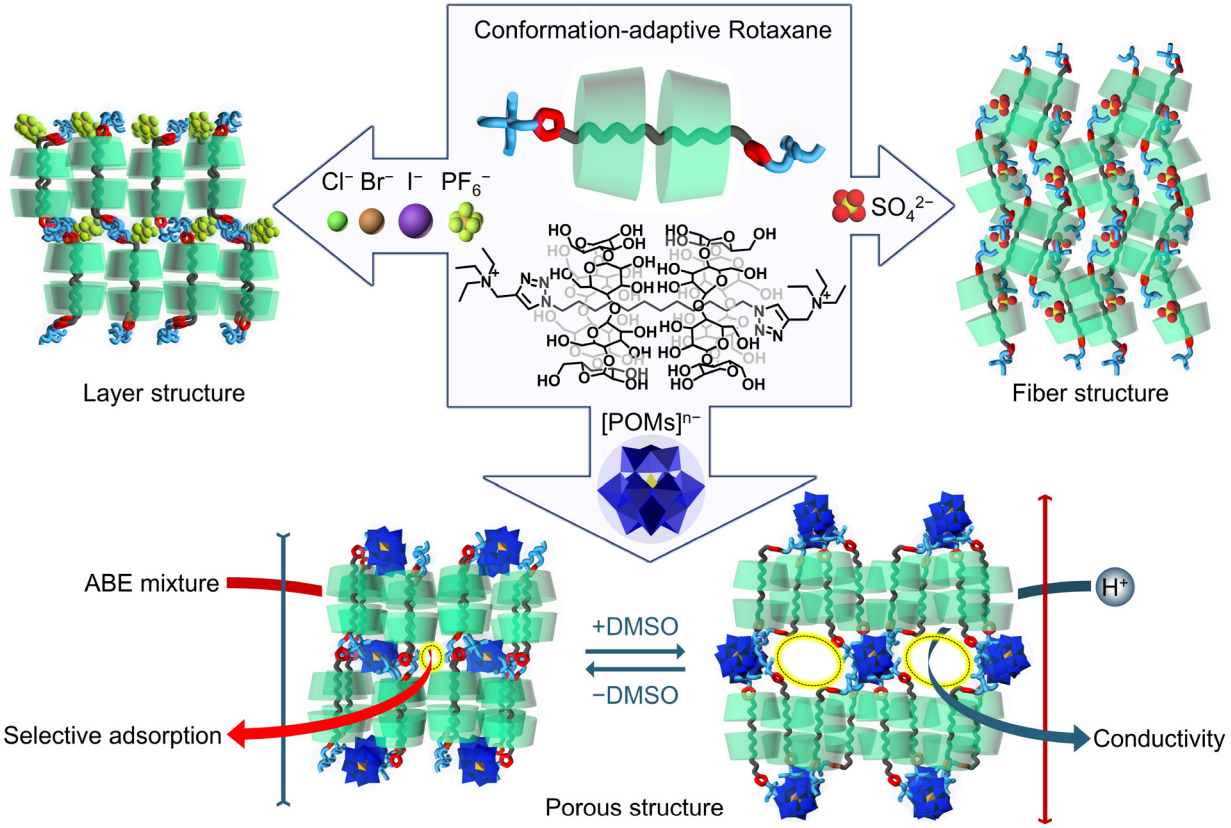

Scheme 1 Regulation of rotaxane structures by assembly with anions to form layered, fibrous, and porous structures. The porous rotaxane assemblies exhibit structural adaptability to solvents, enabling selective adsorption and proton conductivity.

strategy. Rotaxanes, a class of mechanically interlocked molecules (MIMs), consist of multiple molecular components linked through their topological structure, providing themselves with high structural stability and adaptability.[32–36] By designing rod-shaped cyclodextrin[3]rotaxanes (CRs) with a bola-cationic structure, these nanoscale molecules can be spatially matched with POMs and form expected assembly structures by adjusting the anions, making them ideal complementary nanocationic linking groups for POMs.

In this context, our concept is to combine the bola-cationic rotaxanes electrostatically with large anionic clusters, utilizing the chaotropic effect[37,38] from electrostatic interactions to form stable porous rotaxane assemblies (PRAs). Lateral hydrogen bonding in rod-shaped rotaxanes induces their dense packing, leading to the formation of a layered structure. The multicharged nature and small nanoscale POMs enable them to align directionally within the ionic layers, thereby forming a regular pore structure. The PRAs exhibit a unique "breathing effect", where the pore structure undergoes reversible adjustments during the adsorption and desorption processes in polar or amphiphilic solvents. This behavior is demonstrated in efficient adsorption and separation of butanol and acetone in acetone–butanol–ethanol (ABE) mixtures. DMSO can disrupt the hydrogen bonds and ionic interactions in PRAs, causing them to recrystallize in DMSO/H_2O solution and form a porous single crystal structure with larger pore sizes. The changes in the pore structures lead to the diversification of the hydrogen bond network, which significantly enhances proton conductivity (Scheme 1). As a result, this solution ensures the formation of porous supramolecular assemblies and highlights the adaptability of rotaxanes and the flexibility of ionic bonds. The method demonstrated here holds great potential for the assembly and application of series of nanoclusters with multi-head-bridging nanoscale cations.

2. Experimental section

2.1 Synthesis and ion change of rotaxane

The full synthesis route is presented in the ESI.†

2.1.1 CR·SO_4. 1,12-Diazidododecane was dropwise added to an aqueous solution of α-cyclodextrin and then stirred with ultrasound for 1 hour to obtain a viscous white turbid solution. Aqueous solutions of triethylpropargylammonium bromide, $CuSO_4$, and sodium ascorbate were added successively and then pentamethyldiethylenetriamine was added dropwise. The mixture was stirred at room temperature for 90 hours, the precipitate was removed and the solution was concentrated by rotary evaporation. A large amount of acetone was added to the concentrated aqueous solution to separate a

pale blue powder. The crude product was further purified using Sephadex G-25 several times and recrystallized in MeOH/H_2O. CR·SO_4 was obtained as a white powder in 16.23% yield. Ethanol vapor was slowly volatilized into the CR·SO_4 alkaline aqueous solution, resulting in colorless needle-like or block crystals.

2.1.2 CR·PF_6. CR·SO_4 and KPF_6 were dissolved in water to obtain a clear solution and evaporated for one day to produce colorless block crystals.

2.1.3 CR·Cl/Br/I. CR·SO_4 aqueous solution was treated with activated ion exchange resins (by NaCl/NaBr/NaI) for one day. The resins were removed by filtration and the ion-substituted CR was precipitated in acetone. Ethanol vapor was slowly volatilized into the CR·Cl/Br/I alkaline aqueous solution, resulting in colorless needle-like or block crystals.

2.1.4 CR·POM ($SiW/PMo/PMo_{11}V/PMo_{10}V_2/PMo_9V_3$) state A. CR·$SO_4$, POMs, and CH_3COOK were mixed in H_2O, and then CH_3COOH was added to adjust the pH value to about 4. The suspension was transferred to a Teflon-lined reactor and kept at 102 °C for 3 days. The reactor was cooled to room temperature slowly and crystals of CR·POM state A were obtained. The same structural assembly can be built by simply adding dropwise an aqueous solution of CR·SO_4 into an aqueous solution of POMs at 50 °C while stewing for 30 min.

2.1.5 CR·POM ($SiW/PMo/PMo_{11}V/PMo_{10}V_2/PMo_9V_3$) state B. Method 1: A DMSO/H_2O/CH_3COOH solution of CR·SO_4 was added to a DMSO/H_2O/CH_3COOH solution of POMs, and then the mixture was stewed for a few days to obtain needle-like crystals. Method 2: CR·POM assembly powder was dissolved in DMSO, and H_2O was slowly evaporated into it for a few days to obtain needle-like crystals.

2.2 Selective adsorption experiment

2.2.1 Vacuum degassing of the CR·$PMo_{11}V$ assembly. The as-prepared CR·$PMo_{11}V$ assembly powder was vacuum-dried at 100 °C for 4 hours, following which PXRD analysis was performed to confirm the structural changes.

2.2.2 Solvent vapor adsorption. 3 mg of the vacuum-degassed CR·$PMo_{11}V$ assembly was placed in a vial, which was then sealed within a larger vial containing the solvents. The solvent vapor was allowed to gradually diffuse into the powder for 72 hours at room temperature. Subsequently, NMR analysis was conducted to calculate the maximum adsorption amount.

2.2.3 Butanol-selective multicomponent adsorption. Breakthrough experiments of H_2O, ethanol, acetone, and butanol vapors were conducted at a constant temperature of 25 °C using a Micromeritics ASAP 2920 system paired with an HPR-20 R&D mass spectrometer detector. PRAs were accurately weighed and loaded into the experimental setup. The vapor generator's temperature conditions were set to produce the desired model ABE mixture concentrations, consisting of 1 mol% butanol, 0.6 mol% acetone, and 0.25 mol% ethanol in water. The carrier gas (N_2) flow rate was adjusted to 10 mL min^{-1} to ensure a constant gas flow. The sample was then exposed to the target vapor flow, and real-time monitoring of the outlet gas composition was performed to record the breakthrough curves and sample adsorption amounts for each vapor. Following the adsorption experiments, sequential desorption runs were conducted at 453 K to evaluate the material's desorption performance. The adsorption–desorption cycles for the ABE mixture were repeated for three complete cycles to assess the reproducibility.

2.3 Computational details

The relative energy of the CR was performed using the ORCA (version 5.0.4) software package. ORCA is a versatile quantum chemistry program capable of performing various types of calculations, including density functional theory (DFT), Hartree–Fock (HF), and post-HF methods.[39]

Geometry optimizations were carried out using the B97-3C functional with the embedded basis set since the molecules have 350 atoms. To account for dispersion interactions, the DFT-D3 correlation correction was included in the calculations. This correction accounts for the long-range dispersion forces that are not adequately captured by standard DFT functionals. The D3 correction was applied with the Becke–Johnson damping scheme.[40]

The solvation model based on density (SMD) implicit solvation model was applied to account for the solvation effect of water and the mixture of water/DMSO. The built-in parameter for water in SMD was used directly by setting the corresponding keywords. The mixture of water/DMSO was set by the two key parameters of dielectric constant (62.77, average of water and DMSO) and refractivity (1.4095, average of water and DMSO).

The adsorption energy of the anions in the framework of the CR was calculated using the CP2K package (version 7.1) in the framework of semiempirical tight binding methods GFN-xTB and density functional theory.[41,42] The crystals were first optimized at the GFN1-xTB level. Then the binding energies were calculated at the DFT level with the hybrid Gaussian and plan-wave scheme and DZVP-MOLOPT-SR-GTH basis sets. During the calculations, the self-consistent continuum solvation (SCCS) model was used, and the parameters were set to be consistent with the parameters in ORCA.

3. Results and discussion

3.1 Anion-regulated rotaxane assemblies

During the construction of cationic CRs, a pseudo-rotaxane of α-cyclodextrins and 1,12-lauryl diazide in a molar ratio of 2 : 1 is used.[43] Ammonium groups are then grafted to both ends of the alkyl chain diazide through a click reaction, forming a quaternary ammonium-sealed rotaxane (Fig. S1a–g†).[44,45] The mass spectrometry analysis (Fig. S1h†) showed a characteristic peak at m/z = 1238.6, consistent with the 2 : 1 host–guest complex, which together with elemental analysis confirms the inclusion stoichiometry. Peak assignments are verified through COSY and literature studies (Fig. S2†).[46] DOSY measurements revealed a shared diffusion coefficient of 7.48 × 10^{-7} cm^2 s^{-1} for both cyclodextrin and guest molecule protons

(Fig. S3†), confirming the formation of a supramolecular complex. NOESY results also display the correlations between the alkyl chain and cyclodextrin (Fig. S4†), confirming the mechanical locking of cyclodextrins and the guest.

Anions with differences in nanosize and surface charge density influence the assembly process, as outlined in the Hofmeister series.[47–49] By performing ion exchange to obtain complexes with different counterions, the effect of anions on the assembly of CR is systematically investigated. Significant downfield shifts of $H_{OH\text{-}2}$ ($\Delta\delta$ = +0.287 ppm, 5.248 ppm → 5.535 ppm) and $H_{OH\text{-}3}$ ($\Delta\delta$ = +0.374 ppm, 5.502 ppm → 5.876 ppm) on the cyclodextrin secondary face, along with shifts of H_d ($\Delta\delta$ = −0.302 ppm, 8.460 ppm → 8.158 ppm) on the triazole, and H_f ($\Delta\delta$ = +0.110 ppm, 1.833 ppm → 1.943 ppm) on the alkyl chain, confirm host–guest binding. These shifts are further enhanced in the sulfate complex ($H_{OH\text{-}2}$: 6.147 ppm; $H_{OH\text{-}3}$: 6.201 ppm; H_d: 8.045 ppm; H_f: 2.114 ppm) (Fig. S5†). As KPF_6 is gradually added to a DMSO-d_6 solution of CR·SO_4, slow downfield shifts of H_d and upfield of $H_{OH\text{-}2,3}$ are observed, with the shifts correlating with the KPF_6 concentration until the CR : PF_6^- binding ratio reaches 2 : 1 (Fig. S6a and b†). 2D NOESY reveals that in the case of CR·SO_4, $H_{OH\text{-}2,3}$ interacts strongly with water, while in CR·PF_6 these protons show a stronger self-interaction (Fig. S6c†). This result suggests that the sulfates, as kosmotropic ions, disrupt the hydrogen bonds in contrast to the chaotropic PF_6^- which binds to hydrophobic regions of CR. Upon adding PF_6^- to CR·SO_4 solution, it pushes the cyclodextrin pairs apart by exposing triazole groups (Fig. S6d†).

The impact of counterions on the assembly structure has been studied through single-crystal structure analysis. When the anions are simple monocharged ions, such as Cl^-, Br^-, I^-, and PF_6^-, the assembly structures are similar (Tables S1–4†). Part of the alkyl chain of the guest is located slightly outside the cyclodextrin pair, and the rotaxane exhibits minor structural asymmetry (Fig. S7a and b†). The rotaxane arranges into a lamellar structure with a hexagonal array in the inner layer, while the counterions and cationic heads are situated in the middle of two rotaxane layers through electrostatic interactions (Fig. 1a–d, S7c–e†). The rotaxanes are attached in parallel with each other *via* hydrogen bonding between cyclodextrins and crystallization water, with characteristic O···O distances of 2.64–3.21 Å (Fig. S8, Tables S5–7†). When the anion is SO_4^{2-}, the sulfate ion binds with two cations and disrupts the hydrogen bonds within the CR layers through its own hydrogen bonds with the cyclodextrins (O···O: 2.74–2.77 Å), which leads to the transformation of the assembly structure from a layered to a fibrous form (Fig. 1e–h, S9, S10, Tables S8–11†). This is consistent with the conclusions from NMR data and further underscores the strong hydrogen bonding competition ability of sulfate ions.

However, the strong combination of the multiply charged POM clusters with CRs leads to rapid precipitation. The addition of salts enhances the solubility of assemblies in water

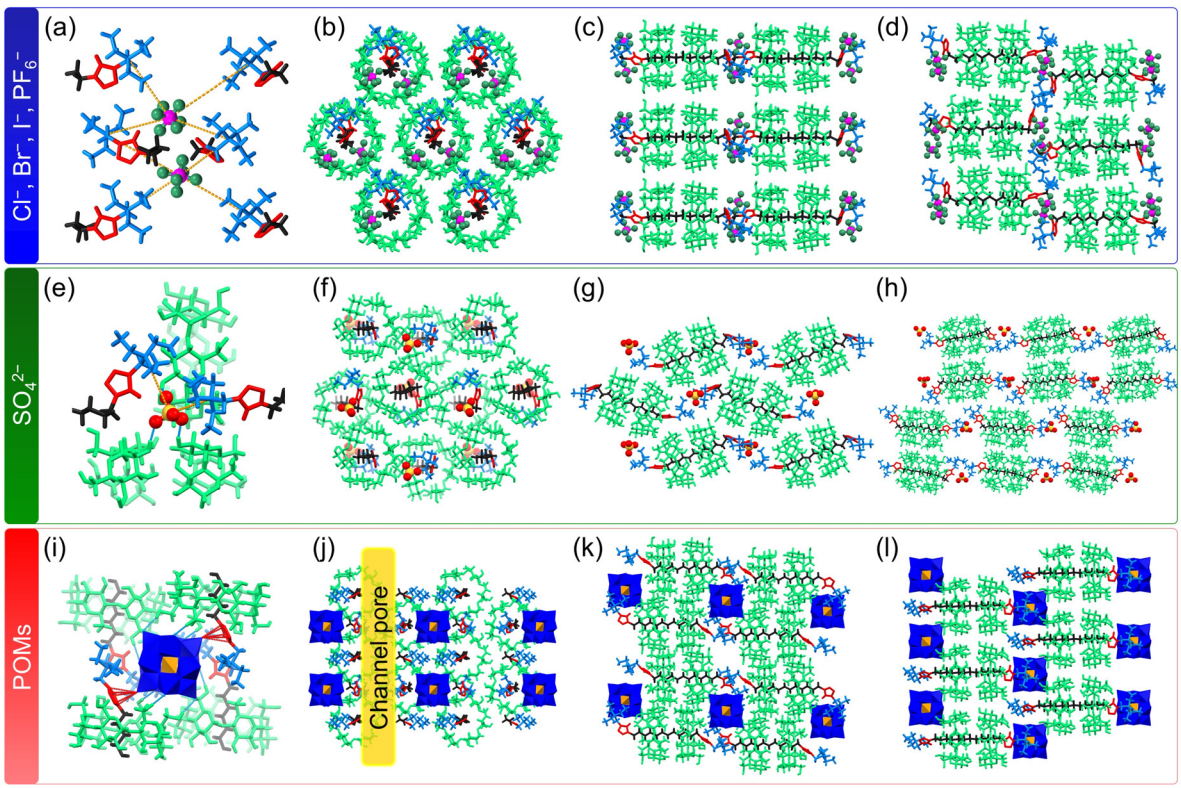

Fig. 1 Different single-crystal structures of rotaxanes with various counterions. (a–d) CR·Cl/Br/I/PF_6 with a layer structure; (e–h) CR·SO_4 with a fiber structure; and (i–l) CR·SiW with a porous structure.

by attenuating the ionic interactions.[50] Using this method, a single crystal was prepared under hydrothermal conditions (Table S12†). CRs and POMs co-assemble into an alternating layered structure, with the cationic CRs exhibiting a hexagonal arrangement, as seen in CR·PF_6. Differently, one cluster interacts electrostatically with six triethylamine groups and engages in anion–π interactions with the triazole group. Each POM strengthens its binding affinity with CRs through hydrogen bonds to cyclodextrins (O···O: 2.87–3.15 Å) (Fig. 1i–l, S11, S12, Tables S13–16†). Due to the multiple charges and larger size of the POM, the cations are bound around it, resulting in the formation of a 1D channel with a diameter of approximately 0.6 nm within the ion layers (Fig. S13†). Solvent masks generated by PLATON indicate that the volume of voids is 870 $Å^3$, occupying about 5.93% of the unit cell. Elemental analysis confirms the presence of 24 free water molecules within the voids (Tables S17 and S18†).

3.2 Construction of porous ionic rotaxane assemblies and selective adsorption

A rotaxane-cluster porous ionic assembly can be rapidly prepared by simply mixing aqueous solutions of POM and CR, resulting in an assembly with a negatively charged surface (Fig. 2a and b). PXRD Pawley refinement confirmed that the structure closely resembles that of the single crystal synthesized *via* the hydrothermal method (Fig. 2c). Scanning electron microscopy (SEM), transmission electron microscopy (TEM), and atomic force microscopy (AFM) images (Fig. 2d–f) reveal the nanorod morphology of the assembly. The high-resolution TEM (HRTEM) image (Fig. 2g) shows that the dark domains corresponding to POMs are arranged linearly. Energy-dispersive X-ray (EDX) spectroscopy mapping further confirms the POMs in the ionic assembly (Fig. 2h). Meanwhile, the Keggin-type POM clusters containing different elements and varying charges assemble into an identical structure with the CR, demonstrating the versatility of this preparation method (Fig. S14†).

Based on the inherent structural flexibility of the ionic assembly, PRAs can display a pronounced "breathing" effect.[51–53] Specifically, when the solvent is removed from the assembly, the structure shifts from an open porous state to a closed porous state. Upon interaction with suitable molecules, the structure can either partially or fully return to its original form (Fig. 3a–c). By analyzing the maximum adsorption capacity of PRAs for different solvent molecules (Fig. S15†), it is evident that hydrophilic polar molecules and certain amphiphilic molecules interact effectively with the assembly, opening the closed pores. In contrast, hydrophobic nonpolar molecules fail to reopen the closed pores, resulting in very low adsorption capacity (Fig. S16–39†). N_2 cannot open the closed

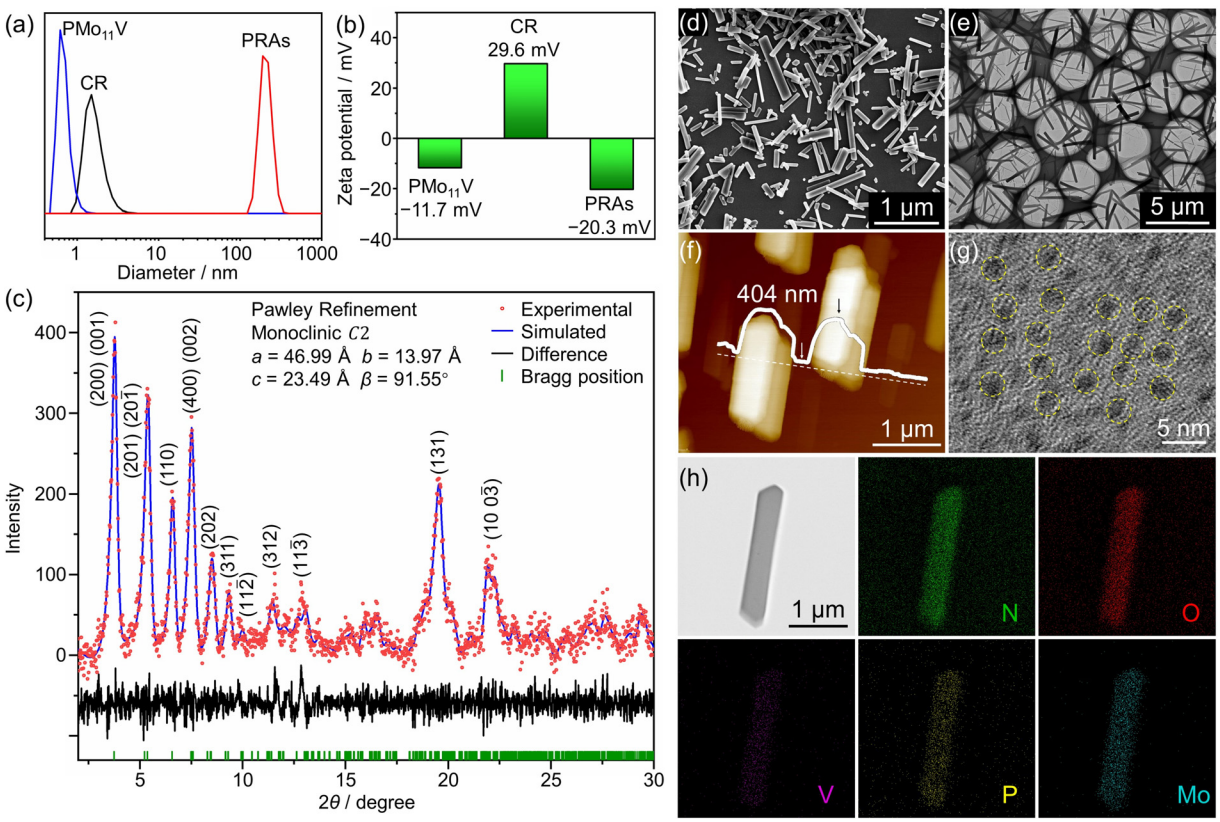

Fig. 2 (a) DLS and (b) zeta potential of $H_4PMo_{11}VO_{40}$ (0.02 mM), CR·SO_4 (0.04 mM), and CR·$PMo_{11}V$ assembly (0.02 mM) aqueous solution. (c) PXRD Pawley refinement of the CR·$PMo_{11}V$ assembly. (d) SEM, (e) TEM, (f) AFM, (g) HRTEM images and (h) elemental mapping of the nano-rod CR·$PMo_{11}V$ assembly.

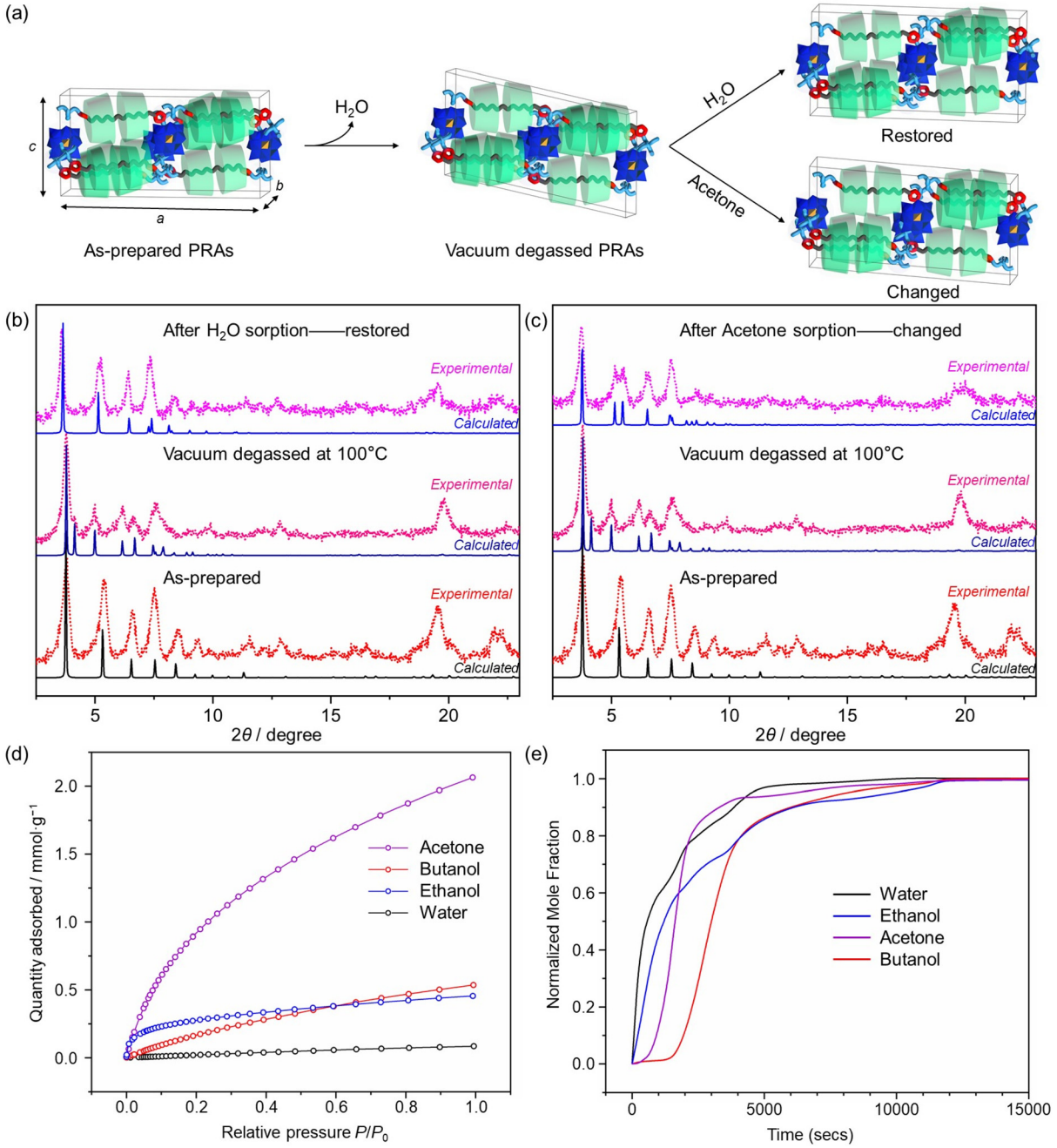

Fig. 3 (a) "Breathing" effect of the CR·$PMo_{11}V$ assembly. Comparison of the PXRD patterns of the CR·$PMo_{11}V$ assembly: as-prepared, vacuum degassed, and after (b) H_2O and (c) acetone sorption. (d) Water, ethanol, acetone, and butanol sorption isotherms of CR·$PMo_{11}V$ assembly. (e) Breakthrough profiles showing the normalized mole fractions at the outlet of the packed-bed adsorber for a sparged mixture from a model ABE mixture.

pores, resulting in larger gas adsorption in the open-porous state. CO_2 adsorption confirms that the pore size is approximately 0.6–0.8 nm, consistent with the single-crystal analysis, thereby confirming the presence of real porous channels (Fig. S40†). These properties make the material suitable for the adsorption and purification of mixtures that are difficult to separate in practical production processes.

Acetone–butanol–ethanol (ABE) fermentation is a traditional industrial process with a history of over 100 years, and is the second largest fermentation industry in the world, after bioethanol fermentation.[54,55] However, the butanol concentration in the fermentation broth is very low, and finding an energy-efficient and cost-effective separation process to recover butanol from dilute aqueous solutions remains a significant challenge.[56] The isothermal adsorption curves have been measured, demonstrating that the PRAs selectively adsorb acetone rather than ethanol, butanol, and water (Fig. 3d), consistent with the NMR results. Additionally, mixed vapor break-

through experiments further demonstrate the porous material's adsorption and selective separation of butanol and acetone under practical production conditions (Fig. 3e). To evaluate the feasibility of product recovery, we analyzed the desorption behavior of the adsorbed butanol-rich CR·$PMo_{11}V$ assembly. Remarkably, even after three consecutive adsorption–desorption cycles, the material retained excellent selectivity toward butanol, highlighting its regeneration capability (Fig. S41†).

3.3 DMSO-driven reversible crystalline transformation and proton conductivity variations

PRAs exhibit a resistant behavior to dissociation in common solvents, except for solvents like DMSO, which disrupts hydrogen bonds and ionic interactions. Using this property, PRAs can be recrystallized with a DMSO/H_2O solution to form a porous single crystal holding larger pores. The obtained crystal belongs to the $P2_1$ space group and displays a different assembly compared to the previous structures (Table S19†). Notably, the cation-to-anions ratio remains unchanged, representing different states of the same complex. The crystalline structures obtained in aqueous solution and DMSO/H_2O solution are named state A and state B, respectively. Variations in POMs with different elements and charges do not affect the crystal structure's homogeneity (Table S20†). Elemental tracking of Mo/V ratios provides insight into the compositional changes of phosphovanadomolybdate mixtures in ionic crystals: state A preserves the precursor cluster stoichiometry through rapid assembly, while state B undergoes controlled V depletion (final Mo/V < 11 : 1) during slow crystallization (Table S21†). These findings unequivocally rule out $[PMo_{11}VO_{40}]^{4-}$ as the sole structural origin, instead establishing that polyprotonated, high-valence P–Mo–V species also participate in the formation of the crystalline structure, retaining some un-ionized protons.[57] CR·$PMo_{11}V$-B features alternating layers of CRs and POMs with a significantly larger layer spacing than CR·$PMo_{11}V$-A due to the insertion of DMSO between POM and cyclodextrin (Fig. S42†) and exhibits a distinct porous topology with a 1D channel of 1.4 nm diameter enclosed within a 2D rhombic framework (Fig. S43†). Solvent masks generated by PLATON reveal that the volume of voids is 3520 $Å^3$, occupying approximately 18.07% of the cell. Thermogravimetric analysis (Fig. S44†) and elemental analysis indicate the presence of solvents filling the void (Tables S21 and 22†). The volume of voids in state B is 4.05 times that of the cavities in state A. The hydrogen bonds between the POM cluster and cyclodextrins (O···O: 2.78–3.10 Å) are significantly reduced due to the occupancy of DMSO molecules at the binding sites with cyclodextrin and POM. There are also hydrogen bonds between two cyclodextrins on the same CR with O···O distances of 2.70–3.07 Å, consistent with the NMR spectrum. Interactions among the secondary face of cyclodextrins and crystalline water become more complicated due to the distortion of the CR pattern. DMSO molecules participate in a hydrogen bonding network with the primary face of cyclodextrins, with more crystalline water molecules found to derive from the larger pores (Fig. S45, Tables S23–26†).

This dramatic change of porous structures obtained in aqueous solution and DMSO/H_2O solution supports the *in situ* transformation between the two crystalline structures. Typically, by immersing in water, state B single crystals turn opaque quickly. The 2D diffraction patterns show that the original diffraction dots transform into diffraction rings, and the diffraction peak at the smallest angle shifts toward a wide angle. This is highly consistent with the diffraction peaks of state A assemblies in water, indicating the transformation between the two well-characterized crystalline structures. By reimpregnating those opaque grains in DMSO/H_2O solution, the first diffraction peak shifts back to its initial state (Fig. S46†). PXRD Pawley refinement further verifies that the solvent environment induces structural changes (Fig. 4a, and S47†). To better understand the reversible structural transformation, the *a* and *c* directions are properly adjusted, and two unit cells are selected, ensuring that the contents are consistent (Fig. 4b). Within the layers of rotaxanes (*a*, *b*-axis), the CRs adopt approximately hexagonal close packing in both states, which results in a minimal variation of the unit cell dimensions. In contrast, accompanied by a rotation of about 16.21°, there is an approximately 33.89% elongation of the unit cell dimensions along the direction (*c*-axis), which is perpendicular to the rotaxane layers.

To further explore the mechanism of structural transformation, IR spectra are conducted. To eliminate interference from KBr, *in situ* attenuated total reflection (ATR) spectroscopy was employed. Compared to state A, in state B, the ν(O–H) vibration peak shifted from 3358 cm^{-1} to 3317 cm^{-1}, while the δ(O–H) bending vibration peak shifted from 1470 cm^{-1} to 1435 cm^{-1} (Fig. S48†). These spectral shifts suggest the strengthening of hydrogen bonding in state B.[58,59] The hydrogen bonds inferred from IR spectra are likely to occur between DMSO and cyclodextrin, which is well supported by the analysis of state B single crystals. In addition, under the influence of DMSO, the conformation of CR changes, with the cyclodextrin pair moving towards one end of the guest molecule to expose more hydrophobic alkyl chains, thereby inhibiting the interaction between the anion and triazole. On the other hand, the number of cations directly interacting with the POM exterior increases from 6 to 8. However, this does not alter the overall charge balance. From the top view of the ion layer, it is evident that the 1D POM chains undergo a rotation of approximately 29.6° on the hexagonally arranged cations. This rotation causes some cation heads, which were previously bonded to only one cluster in state A, to become shared between two adjacent clusters, resulting in a change in the ion coordination number (Fig. S49†). Facet indexing analysis demonstrates that both rod-like crystals A and B share the same growth orientation, with their long axes aligned with the rotaxane lateral arrangement and parallel to the 1D channels (Fig. S50†). By comparing the NMR spectra of CR in D_2O and DMSO-d_6, proton H_d shows negligible chemical shift change in D_2O (8.365 ppm → 8.371 ppm), and significant pertur-

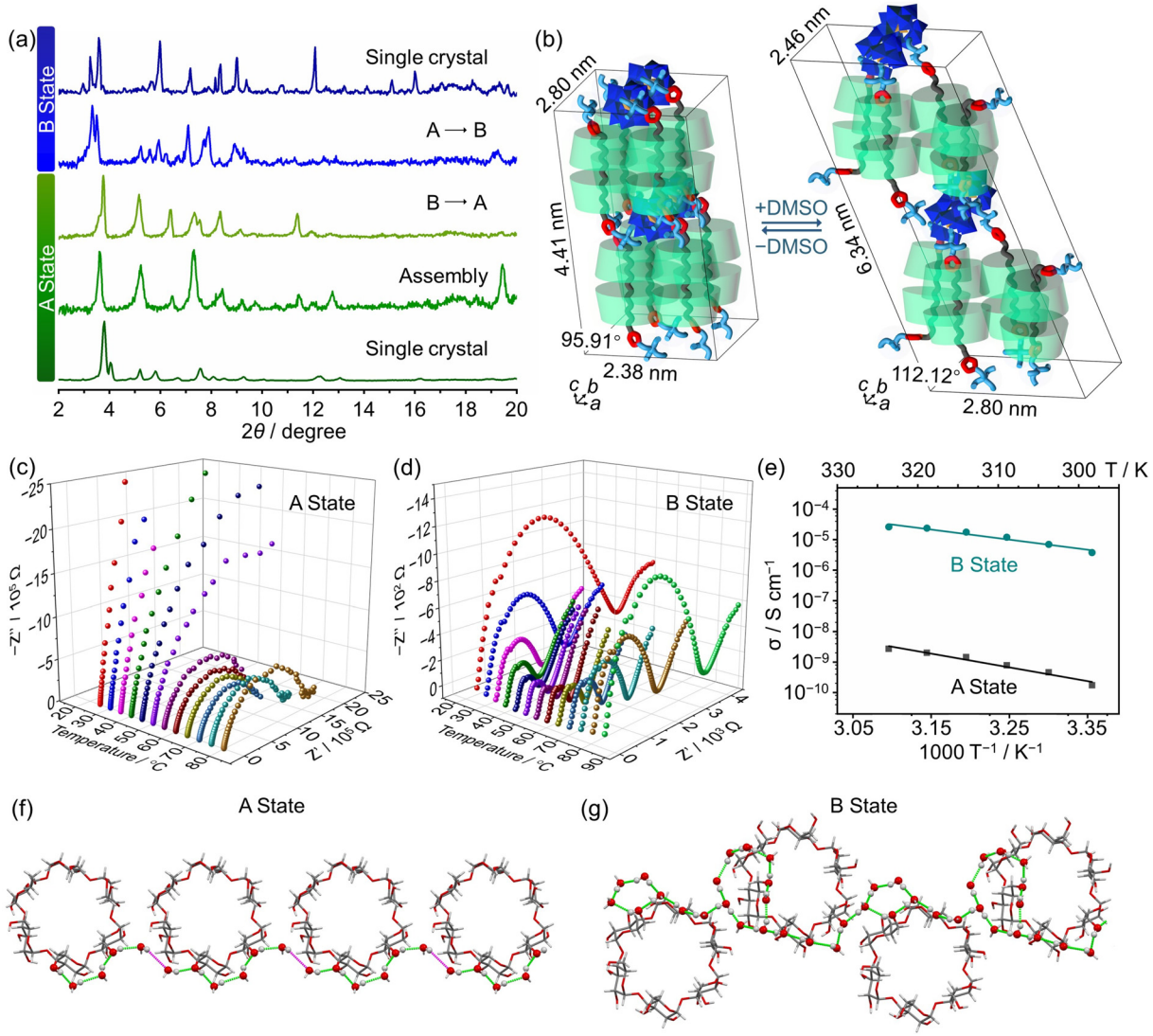

Fig. 4 (a) PXRD comparison of states A and B. (b) Changes in lattice parameters before and after the crystalline transition. Nyquist diagrams of (c) CR·PMo_{11}V-A and (d) CR·PMo_{11}V-B. (e) Comparison of the σ values of states A and B. (f) Unobstructed and (g) truncated proton transport pathways.

bations are observed in DMSO-d_6. This marked contrast confirms a substantial rotaxane conformational rearrangement induced by DMSO (Fig. S51†).

The theoretical simulations based on DFT are used to understand the solvent-driven reversible changes of rotaxanes in frameworks in each crystalline state. First, the initial conformations, designated as A and B (Fig. S52†), are derived from the CR conformation in states A and B. Distributional structure optimization is performed using the ORCA software package in different implicit solvents, which are accounted for using the solvation model based on density (SMD) by adjusting the solvent environment parameters according to dielectric constant and refractivity. Since DFT structure optimization only identifies the local energy minima without allowing for temperature-induced perturbations, the conformations undergo only minor adjustments of bond lengths and angles, with no significant relative movements between host and guest components. Thus, the optimized conformations are considered representative of their states in crystals. As a result, the relatively symmetrical conformation A in water exhibits lower energy, indicating its more stable state with an energy difference of 1.0036 kJ mol^{-1} compared to conformation B. Conversely, the off-centered conformation B of cyclodextrin in DMSO/H_2O (1 : 1 v/v) shows lower energy, suggesting its more stable state with an energy difference of 7.8 kJ mol^{-1} compared to conformation A (Table S27†). This result can be understood as follows: due to the hydrophobic nature of the alkyl chain, its conformation tends to be largely covered by cyclodextrins in an aqueous environment, leading to a lower interfacial energy. On the other hand, the hydrophobicity increase of the environment improves the surrounding affinity, resulting in the exposure of the alkyl chain outside the cyclodextrin, thereby lowering the energy.

In addition to bistable rotaxanes serving as significant drivers of structural changes, ionic interactions under different solvent environments have also been revealed as contributing factors to structural alterations. The calculation of binding energies between clusters and rotaxanes in different implicit solvents provides the evidence. Specifically, the crystal structures of A and B are optimized using CP2K software. The total energies of the complete crystal, the crystal with removed anionic clusters, and the individual anionic clusters are calculated using the DFT/PBE functional approximation in various solvents. The binding energies are then determined using the formula "$E_{abs} = E_{tot} - E_{vac} - 2E_{ion}$", where E_{tot} refers to the total energy of the unit cell, E_{vac} denotes the total energy of the unit cell excluding two anion clusters, E_{ion} represents the energy of a single anion cluster, and E_{abs} signifies the binding energy between the anion cluster and rotaxane and the solvent in the crystal (Tables S28 and S29†). In the state A structure, the binding energy between anionic clusters and rotaxanes is relatively higher in water compared to that in DMSO/H_2O, whereas in the state B structure, the opposite conclusion is reached (Fig. S53†). These comparisons indicate the presence of bistable binding modes between POM and rotaxanes in response to the solvent change, which drives the structural transition process along with the rotaxane motions.

POMs act as proton carriers for proton conductivity, with POM-containing porous ionic crystals showing this property.[60–62] To illustrate the modulation of structural transformation for conductivity performance,[63] electrochemical impedance spectroscopy was performed. State A yields a conductivity of 6.72×10^{-9} S cm^{-1}, while that of state B increases to 2.85×10^{-5} S cm^{-1}, showcasing a difference as significant as 4000 times (Fig. 4c–e), which can be explained by the richer hydrogen bonding network in state B compared to state A, where multiple hydrogen-bonding pathways enhance proton transport (Fig. 4f and g). The conductivity increases linearly with temperature up to 50 °C, with an activation energy of 0.798 eV, suggesting a vehicle mechanism.[64] When the temperature exceeds 55 °C, the conductivity decreases, suggesting the collapse of the hydrogen bonding network (Fig. S54a–c†). As the charge numbers (3–6) of the POMs do not influence the structure, $[PMo_9V_3O_{40}]^{6-}$ is chosen for the study. Extra protons that are not replaced remain in the formed channels. The proton conductivity test receives a σ value of 3.67×10^{-4} S cm^{-1}, which is 12.9 times higher than that of CR·PMo_{11}V-B (Fig. S54d and e†).

4. Conclusions

In conclusion, through a strategy of molecular design and the regulation of rotaxane structures assembled with polyanionic nanoclusters, porous organic–inorganic hybrid assemblies bearing one- and two-dimensional channels have been successfully prepared based on ionic interactions and size matching. The intermolecular framework structure and flexible ion-binding of nanosized nodes in the surrounding polarity environment impart solvent adaptability to the porous assembly, thus enabling selective adsorption of mixed liquids. This kind of innovative ionic composite material shows a unique potential for separations such as enriching butanol from ABE mixtures and holds promise for exhibiting tunable properties in proton conduction applications.

Author contributions

J. W. designed and conducted the experiments and wrote the manuscript; M. W. and Z. Z. contributed to the discussion; B. L. and L. W. directed the project. All the authors contributed to this work.

Data availability

The data supporting this article have been included as part of the ESI.†

Conflicts of interest

There are no conflicts to declare.

Acknowledgements

The authors gratefully acknowledge the support from the National Natural Science Foundation of China (22271117 and 22172060).

References

1 X. Tang, J. Pang, J. Dong, Y. Liu, X.-H. Bu and Y. Cui, Supramolecular assembly frameworks (SAFs): shaping the future of functional materials, *Angew. Chem., Int. Ed.*, 2024, **63**, e202406956.
2 Z. Sun, R. Wang and I. V. Kozhevnikov, Versatile POMOF-based materials: synthesis, mechanism, topology and catalytic applications, *Coord. Chem. Rev.*, 2025, **524**, 216304.
3 G. Liu, S. Li, C. Shi, M. Huo and Y. Lin, Progress in research and application of metal–organic gels: a review, *Nanomaterials*, 2023, **13**, 1178.
4 H.-M. Zeng, X.-J. Wang, Z.-G. Jiang and C.-H. Zhan, Polyoxometalate-based frameworks as chemical nanoreactors: *in situ* synthesis of active silver nanoparticles in confined spaces, *Inorg. Chem. Front.*, 2024, **11**, 1207–1213.
5 Y. Jin, Q. Wang, P. Taynton and W. Zhang, Dynamic covalent chemistry approaches toward macrocycles, molecular cages, and polymers, *Acc. Chem. Res.*, 2014, **47**, 1575–1586.
6 K. Liu, C. Ma, T. Wu, W. Qi, Y. Yan and J. Huang, Recent advances in assemblies of cyclodextrins and amphiphiles: construction and regulation, *Curr. Opin. Colloid Interface Sci.*, 2020, **45**, 44–56.

7 R. X. Bai, X. Yang, J. Zhao, Z. M. Zhang and X. Z. Yan, Phototriggered formation of a supramolecular polymer network based on orthogonal H-boding and host-guest recognition, *Chem. Res. Chin. Univ.*, 2023, **39**, 777–781.
8 E. Raee, B. Liu, Y. Yang, T. Namani, Y. Cui, N. Sahai, X. Li and T. Liu, Side group of hydrophobic amino acids controls chiral discrimination among chiral counterions and metal–organic cages, *Nano Lett.*, 2022, **22**, 4421–4428.
9 J. Yu, J. Niu, X. Xu and Y. Liu, Configurationally stepping confinement achieved tunable chiral near-infrared luminescence supramolecular phenothiazine organic framework, *Adv. Sci.*, 2024, **11**, 2408107.
10 L. Zhang, C. Y. Zhang, J. Min, C. L. Liu, S. Z. Mao, L. Y. Wang, B. Yang and Z. Y. Dong, A general approach for synthesis of circularly assembled supramolecular polymers by means of region-confined amphiphilic supramolecular polymerization, *Chem. Res. Chin. Univ.*, 2023, **39**, 736–740.
11 Z.-Q. Li, J.-Y. Shao, Z.-L. Gong, T. Liang, X. Hao, J. Yao and Y.-W. Zhong, Self-healing 2D anion-organic frameworks for low-temperature water release, *Angew. Chem., Int. Ed.*, 2025, **64**, e202419096.
12 X. H. Li, X. D. Li, Q. H. Sun, J. J. He, Z. Yang, J. C. Xiao and C. S. Huang, Synthesis and applications of graphdiyne derivatives, *Acta Phys.-Chim. Sin.*, 2023, **39**, 2206029.
13 Y. Xie, X. Ding, J. Wang and G. Ye, Hydrogen-bonding assembly meets anion coordination chemistry: framework shaping and polarity tuning for xenon/krypton separation, *Angew. Chem., Int. Ed.*, 2023, **62**, e202313951.
14 R. Eguchi, S. Uchida and N. Mizuno, Inverse and high CO_2/C_2H_2 sorption selectivity in flexible organic–inorganic ionic crystals, *Angew. Chem., Int. Ed.*, 2012, **51**, 1635–1639.
15 I. Hutskalov, A. Linden and I. Čorić, Directional ionic bonds, *J. Am. Chem. Soc.*, 2023, **145**, 8291–8298.
16 J.-X. Liu, X.-B. Zhang, Y.-L. Li, S.-L. Huang and G.-Y. Yang, Polyoxometalate functionalized architectures, *Coord. Chem. Rev.*, 2020, **414**, 213260.
17 M. Sadakane and E. Steckhan, Electrochemical properties of polyoxometalates as electrocatalysts, *Chem. Rev.*, 1998, **98**, 219–238.
18 S. Chai, R. Zhong, L. Zhai, H. Guo, X. Li, L. Wu and H. Li, A soft processible polyoxometalate-zwitterion eutectic electrolyte for superprotonic conduction, *Fundam. Res.*, 2023, DOI: 10.1016/j.fmre.2023.09.003.
19 Y. Wang, O. Zeiri, M. Raula, B. Le Ouay, F. Stellacci and I. A. Weinstock, Host–guest chemistry with water-soluble gold nanoparticle supraspheres, *Nat. Nanotechnol.*, 2017, **12**, 170–176.
20 G. Xing, T. Yan, S. Das, T. Ben and S. Qiu, Synthesis of crystalline porous organic salts with high proton conductivity, *Angew. Chem., Int. Ed.*, 2018, **57**, 5345–5349.
21 S. Yu, G.-L. Xing, L.-H. Chen, T. Ben and B.-L. Su, Crystalline porous organic salts: from micropore to hierarchical pores, *Adv. Mater.*, 2020, **32**, 2003270.
22 J.-H. Son, H. Choi and Y.-U. Kwon, Porous crystal formation from polyoxometalate building blocks: single-crystal structure of $[AlO_4Al_{12}(OH)_{12}(H_2O)_{24}]$ $[Al(OH)_6Mo_6O_{18}]_2$ $(OH)\cdot 29.5H_2O$, *J. Am. Chem. Soc.*, 2000, **122**, 7432–7433.
23 S. Uchida, M. Hashimoto and N. Mizuno, A breathing ionic crystal displaying selective binding of small alcohols and nitriles: $K_3[Cr_3O(OOCH)_6(H_2O)_3][\alpha\text{-}SiW_{12}O_{40}]\cdot 16H_2O$, *Angew. Chem., Int. Ed.*, 2002, **41**, 2814–2817.
24 W. Tian, L. Guo, H. Hu, J. Chu, L. He and Y.-F. Song, Frontiers and applications of polyoxometalates-based porous ionic crystals, *Chin. Sci. Bull.*, 2022, **67**, 655.
25 L. Yue, S. Wang, D. Zhou, H. Zhang, B. Li and L. Wu, Flexible single-layer ionic organic–inorganic frameworks towards precise nano-size separation, *Nat. Commun.*, 2016, **7**, 10742.
26 G. Zhang, B. Li, Y. Zhou, X. Chen, B. Li, Z.-Y. Lu and L. Wu, Processing supramolecular framework for free interconvertible liquid separation, *Nat. Commun.*, 2020, **11**, 425.
27 G. Wang, B. Li, B. Li and L. Wu, Gold nanocrystal-loaded 2D supramolecular network for plasmon-enhanced nitrogen fixation, *Green Chem.*, 2023, **25**, 10556–10566.
28 M. Wei, B. Li and L. Wu, Structure transformation and morphologic modulation of supramolecular frameworks for nanoseparation and enzyme loading, *Adv. Sci.*, 2023, **10**, 2207047.
29 Y. Zhang, G. Zhang, B. Li and L. Wu, Non-stop switching separation of superfine solid/liquid dispersed phases in oil and water systems using polymer-assisted framework fiber membranes, *Small Methods*, 2023, **7**, 2201455.
30 M. Wei, F. Duan, B. Li, Y. Wang and L. Wu, *In situ* grown coordination-supramolecular layer holding 3D charged channels for highly reversible Zn anodes, *Nano Lett.*, 2024, **24**, 4124–4131.
31 Y. Zhang, B. Li and L. Wu, GO-assisted supramolecular framework membrane for high-performance separation of nanosized oil-in-water emulsions, *Acta Phys.-Chim. Sin.*, 2024, **40**, 2305038.
32 J. F. Stoddart, Mechanically interlocked molecules (MIMs)—molecular shuttles, switches, and machines (nobel lecture), *Angew. Chem., Int. Ed.*, 2017, **56**, 11094–11125.
33 S. Mena-Hernando and E. M. Pérez, Mechanically interlocked materials. rotaxanes and catenanes beyond the small molecule, *Chem. Soc. Rev.*, 2019, **48**, 5016–5032.
34 H. He, E. M. Sevick and D. R. M. Williams, Fast switching from isotropic liquids to nematic liquid crystals: rotaxanes as smart fluids, *Chem. Commun.*, 2015, **51**, 16541–16544.
35 H. He, E. M. Sevick and D. R. M. Williams, Isotropic and nematic liquid crystalline phases of adaptive rotaxanes, *J. Chem. Phys.*, 2016, **144**, 124901.
36 A. Ryabchun, R. Jamagne, J. Echavarren, M. Patanapongpibul, L. Zhang, N. Katsonis and D. A. Leigh, Macroscopic spiral rotation of microscopic objects induced by nanoscale rotaxane dynamics, *Chem*, 2024, **10**, 2196–2206.
37 S. Khlifi, J. Marrot, M. Haouas, W. E. Shepard, C. Falaise and E. Cadot, Chaotropic effect as an assembly motif to construct supramolecular cyclodextrin–polyoxometalate-based frameworks, *J. Am. Chem. Soc.*, 2022, **144**, 4469–4477.
38 M. Lion, J. Marrot, W. Shepard, N. Leclerc, M. Haouas, E. Cadot and C. Falaise, Cyclic oxothiomolybdates: build-

ing blocks for cyclodextrin-based open frameworks, *ChemPlusChem*, 2025, **90**, e202400475.
39 F. Neese, Software update: The ORCA program system—version 5.0, *Wiley Interdiscip. Rev.:Comput. Mol. Sci.*, 2022, **12**, e1606.
40 S. Grimme, J. Antony, S. Ehrlich and H. Krieg, A consistent and accurate *ab initio* parametrization of density functional dispersion correction (DFT-D) for the 94 elements H–Pu, *J. Chem. Phys.*, 2010, **132**, 154104.
41 C. Bannwarth, S. Ehlert and S. Grimme, GFN2-xTB—an accurate and broadly parametrized self-consistent tight-binding quantum chemical method with multipole electrostatics and density-dependent dispersion contributions, *J. Chem. Theory Comput.*, 2019, **15**, 1652–1671.
42 J. Hutter, M. Iannuzzi, F. Schiffmann and J. VandeVondele, CP2K: atomistic simulations of condensed matter systems, *Wiley Interdiscip. Rev.:Comput. Mol. Sci.*, 2014, **4**, 15–25.
43 Y. Akae, H. Okamura, Y. Koyama, T. Arai and T. Takata, Selective synthesis of a [3]rotaxane consisting of size-complementary components and its stepwise deslippage, *Org. Lett.*, 2012, **14**, 2226–2229.
44 J. W. Fredy, J. Scelle, G. Ramniceanu, B.-T. Doan, C. S. Bonnet, É. Tóth, M. Ménand, M. Sollogoub, G. Vives and B. Hasenknopf, Mechanostereoselective one-pot synthesis of functionalized head-to-head cyclodextrin [3]rotaxanes and their application as magnetic resonance imaging contrast agents, *Org. Lett.*, 2017, **19**, 1136–1139.
45 H. Sun, J. Han and C. Gao, High yield production of high molecular weight poly(ethylene glycol)/α-cyclodextrin polyrotaxanes by aqueous one-pot approach, *Polymer*, 2012, **53**, 2884–2889.
46 H.-J. Schneider, F. Hacket, V. Rüdiger and H. Ikeda, NMR studies of cyclodextrins and cyclodextrin complexes, *Chem. Rev.*, 1998, **98**, 1755–1786.
47 K. D. Collins, Ions from the Hofmeister series and osmolytes: effects on proteins in solution and in the crystallization process, *Methods*, 2004, **34**, 300–311.
48 A. Salis and B. W. Ninham, Models and mechanisms of Hofmeister effects in electrolyte solutions, and colloid and protein systems revisited, *Chem. Soc. Rev.*, 2014, **43**, 7358–7377.
49 B. Kang, H. Tang, Z. Zhao and S. Song, Hofmeister series: insights of ion specificity from amphiphilic assembly and interface property, *ACS Omega*, 2020, **5**, 6229–6239.
50 T. Bian, A. Gardin, J. Gemen, L. Houben, C. Perego, B. Lee, N. Elad, Z. Chu, G. M. Pavan and R. Klajn, Electrostatic co-assembly of nanoparticles with oppositely charged small molecules into static and dynamic superstructures, *Nat. Chem.*, 2021, **13**, 940–949.
51 G. Férey and C. Serre, Large breathing effects in three-dimensional porous hybrid matter: facts, analyses, rules and consequences, *Chem. Soc. Rev.*, 2009, **38**, 1380–1399.
52 S. Horike, S. Shimomura and S. Kitagawa, Soft porous crystals, *Nat. Chem.*, 2009, **1**, 695–704.
53 M. Savastano, C. Bazzicalupi and A. Bianchi, Porous frameworks based on supramolecular ball joints: bringing flexibility to ordered 3D lattices, *Chem. – Eur. J.*, 2020, **26**, 5994–6005.
54 I. Veza, M. F. Muhamad Said and Z. A. Latiff, Recent advances in butanol production by acetone-butanol-ethanol (ABE) fermentation, *Biomass Bioenergy*, 2021, **144**, 105919.
55 S. Xie, Z. Li and W. Zhang, Techno-economic analysis of upgrading corn stover-based acetone, *n*-butanol, and ethanol to higher ketones and alcohols: fuels or fine chemicals?, *ACS Sustainable Chem. Eng.*, 2023, **11**, 3474–3485.
56 S. Bhattacharyya, K. C. Jayachandrababu, Y. Chiang, D. S. Sholl and S. Nair, Butanol separation from humid CO_2-containing multicomponent vapor mixtures by zeolitic imidazolate frameworks, *ACS Sustainable Chem. Eng.*, 2017, **5**, 9467–9476.
57 V. F. Odyakov, E. G. Zhizhina, Y. A. Rodikova and L. L. Gogin, Mo-V-phosphoric heteropoly acids and their salts: aqueous solution preparation – challenges and perspectives, *Eur. J. Inorg. Chem.*, 2015, **2015**, 3618–3631.
58 D. L. Thompson, K. B. Wagener, U. Schulze, B. Voit, D. Jehnichen and M. Malanin, Spectroscopic examinations of hydrogen bonding in hydroxy-functionalized ADMET chemistry, *Macromol. Rapid Commun.*, 2015, **36**, 60–64.
59 S. Knop, T. L. C. Jansen, J. Lindner and P. Vöhringer, On the nature of OH-stretching vibrations in hydrogen-bonded chains: pump frequency dependent vibrational lifetime, *Phys. Chem. Chem. Phys.*, 2011, **13**, 4641–4650.
60 N. Osamu, K. Teruo, O. Isao and M. Yoshizo, High-conductivity solid proton conductors: dodecamolybdophosphoric acid and dodecatungstophosphoric acid crystals, *Chem. Lett.*, 1979, **8**, 17–18.
61 K. Niinomi, S. Miyazawa, M. Hibino, N. Mizuno and S. Uchida, High proton conduction in crystalline composites based on Preyssler-type polyoxometalates and polymers under nonhumidified or humidified conditions, *Inorg. Chem.*, 2017, **56**, 15187–15193.
62 J.-X. Wang, Y.-D. Wang, M.-J. Wei, H.-Q. Tan, Y.-H. Wang, H.-Y. Zang and Y.-G. Li, Inorganic open framework based on lanthanide ions and polyoxometalates with high proton conductivity, *Inorg. Chem. Front.*, 2018, **5**, 1213–1217.
63 S. Deng, T. H. Yan, M. Wang, J. Y. Liu, R. H. Deng and J. T. Zhu, Block copolymer particles with tunable and robust internal nanostructures by combining hydrogen-bonding and crosslinking, *Supramol. Mater.*, 2023, **2**, 100034.
64 K.-D. Kreuer, Proton conductivity:materials and applications, *Chem. Mater.*, 1996, **8**, 610–641.

